

THE MAGELLAN EVOLUTION OF GALAXIES SPECTROSCOPIC AND ULTRAVIOLET REFERENCE ATLAS (MEGASaURA) I: THE SAMPLE AND THE SPECTRA

J. R. RIGBY¹, M. B. BAYLISS², K. SHARON³, M. D. GLADDERS^{4,5}, J. CHISHOLM⁶, H. DAHLE⁷, T. JOHNSON³,
R. PATERNO-MAHLER³, E. WUYTS⁸, AND D. D. KELSON⁹

Submitted to ApJ 26 June 2017. Re-resubmitted 31 Oct 2017.

ABSTRACT

We introduce Project MEGASaURA: The Magellan Evolution of Galaxies Spectroscopic and Ultraviolet Reference Atlas. MEGASaURA comprises medium-resolution, rest-frame ultraviolet spectroscopy of $N = 15$ bright gravitationally lensed galaxies at redshifts of $1.68 < z < 3.6$, obtained with the MagE spectrograph on the Magellan telescopes. The spectra cover the observed-frame wavelength range $3200 < \lambda_o < 8280 \text{ \AA}$; the average spectral resolving power is $R = 3300$. The median spectrum has a signal-to-noise ratio of $SNR = 21$ per resolution element at 5000 \AA . As such, the MEGASaURA spectra have superior signal-to-noise-ratio and wavelength coverage compared to what COS/*HST* provides for starburst galaxies in the local universe. This paper describes the sample, the observations, and the data reduction. We compare the measured redshifts for the stars, the ionized gas as traced by nebular lines, and the neutral gas as traced by absorption lines; we find the expected bulk outflow of the neutral gas, and no systemic offset between the redshifts measured from nebular lines and the redshifts measured from the stellar continuum. We provide the MEGASaURA spectra to the astronomical community through a data release.

Keywords: galaxies: evolution—galaxies: high-redshift—gravitational lensing: strong

1. INTRODUCTION

A major driver for the construction of 20 to 30 m optical telescopes is the desire to obtain rest-frame ultraviolet (UV) spectral diagnostics for large numbers of galaxies over most of cosmic time (Skidmore et al. 2015). Rest-frame ultraviolet spectra constrain the hot stellar populations in galaxies via P Cygni stellar wind profiles, and constrain the nucleosynthetic buildup of heavy elements through nebular emission lines (measuring metallicity in the H II regions) and weak photospheric absorption lines (measuring metallicity in the hot stars, c.f. Pettini et al. 2000.)

Rest-frame UV spectroscopy also reveals galactic-scale winds: the mass outflow rate, the velocity structure, ionization structure, metallicity, and abundance pattern of the outflowing gas (Pettini et al. 2002; Quider et al. 2009, 2010). These winds are the famous “galactic feedback” (Heckman et al. 1990, 2000; Veilleux et al. 2005; Martin 2005)—they drive metals into the intergalactic medium, and they may shut down future star formation. In addition, these wavelengths feature a number of emission

lines, most of them weak, that act as spectral diagnostics of the electron temperature, ionization parameter, and abundance pattern (Bayliss et al. 2014)

However, with current telescopes, it has been extremely challenging to obtain, for individual galaxies, both the high signal-to-noise ratios and moderate spectral resolution ($R \sim 3000$) required to make full use of the rest-frame ultraviolet diagnostics. For example, the high-quality, $R=750$ spectrum analyzed by Erb et al. (2010) required 15 hr of integration on Keck; still, this is lower spectral resolution than is ideal for narrow features like photospheric absorption lines. An alternate approach has been to stack the spectra of field (unlensed) galaxies (for example, Shapley et al. 2003; Jones et al. 2012; Steidel et al. 2016; Zhu et al. 2015). The main risks of stacking are that it can be influenced by outliers, and that it washes out heterogeneity within the sample being stacked. In addition, stacks published to date have had lower spectral resolving power ($R = 560, 660, 1400, \text{ and } 2000$ for the four citations above) than is ideal.

A third approach, the one adopted in this paper, is to take advantage of rare cases where galaxies have been highly magnified by gravitational lensing. For the brightest lensed galaxies, medium-resolution rest-frame ultraviolet spectroscopy can be obtained in reasonable integration times with 6-10 m telescopes. By targeting such bright lensed galaxies, spectra can be obtained with current telescopes that can independently measure metallicities for the hot stars, the interstellar medium, and the H II regions within individual galaxies. Such multiple constraints enable vital cross-checks of the bright rest-optical metallicity diagnostics (Steidel et al. 2016), whose empirical calibrations should evolve with redshift (Kewley & Ellison 2008).

To date, only five strongly lensed $z \sim 2-3$ galaxies have been dissected with high-quality rest-frame

Electronic address: Jane.Rigby@nasa.gov

¹ Astrophysics Science Division, Goddard Space Flight Center, 8800 Greenbelt Rd., Greenbelt, MD 20771 USA

² MIT Kavli Institute for Astrophysics and Space Research, 77 Massachusetts Ave., Cambridge, MA 02139 USA

³ Department of Astronomy, University of Michigan, 500 Church St., Ann Arbor, MI 48109 USA

⁴ Department of Astronomy & Astrophysics, University of Chicago, 5640 S. Ellis Ave., Chicago, IL 60637 USA

⁵ Kavli Institute for Cosmological Physics, University of Chicago, 5640 South Ellis Ave., Chicago, IL 60637 USA

⁶ Department of Astronomy, University of Geneva, Geneva, Switzerland

⁷ Institute of Theoretical Astrophysics, University of Oslo, P.O. Box 1029, Blindern, NO-0315 Oslo, Norway

⁸ ArmenTeKort, Antwerp, Belgium

⁹ The Observatories, Carnegie Institution for Science, 813 Santa Barbara St., Pasadena, CA 91101 USA

UV spectroscopy: cB58 (Pettini et al. 2000, 2002); FORJ0332–3557 (Cabanac et al. 2008); the Cosmic Horseshoe (Quider et al. 2009); the Cosmic Eye (Quider et al. 2010); and the Eight O’clock arc (Dessauges-Zavadsky et al. 2011). Each galaxy measured to date has very different outflow properties (Quider et al. 2010); clearly, the published sample size is simply too small to characterize outflows and massive star content at $z \sim 2\text{--}3$.

To directly address this problem, we have conducted Project MEGaSaURA: The Magellan Evolution of Galaxies Spectroscopic and Ultraviolet Reference Atlas. MEGaSaURA has obtained rest-UV spectra of $N = 15$ bright lensed galaxies, taken with the MagE instrument on the Magellan telescopes. This is the sample and data paper for MEGaSaURA, in which we describe the observations and the spectra. We also measure the velocity offsets between the nebulae, stars, and interstellar media within these lensed galaxies.

2. METHODS

2.1. The sample

The MEGaSaURA sample is comprised of $N = 15$ bright strongly-lensed galaxies, spanning the redshift range $1.68 < z < 3.6$, including many of the brightest lensed galaxies known. The criteria for target selection were: highly-magnified lensed galaxies, as bright as possible in the observed g-band, with an image plane configuration such that a significant portion of the total emission would fit into a $10''$ MagE slit with room for sky on both ends of the slit, with a redshift such that both Ly α and C IV are observable by MagE, and at a sufficiently southern declination to be observable by Magellan.

Most of the MEGaSaURA targets are behind cluster-scale lenses that were discovered through two related surveys: SDSS Giant Arcs Survey 1 (SGAS1, Gladders et al. in prep.), and SDSS Giant Arcs Survey 2 (SGAS2, Dahle et al. in prep.) SGAS1 has yielded 217 lenses, with a median giant arc redshift of $z = 2$ (Bayliss et al. 2011; Bayliss 2012); SGAS2 expanded the search space within the Sloan Digital Sky Survey (SDSS), resulting in the discovery of 62 additional lenses.

We also included three targets from other samples: the bright lensed galaxy RCS-GA 032727–132609 (Wuyts et al. 2010), which was discovered through the Red-sequence Cluster Survey-2 (RCS-2, Gilbank et al. 2011); and two bright galaxy-scale lenses: the Cosmic Eye (Smail et al. 2007) and the Cosmic Horseshoe (Belokurov et al. 2007).

Table 1 lists the discovery paper for each arc; several targets were independently discovered by multiple groups. Table 2 lists oxygen abundances as known for the sample; 7 galaxies have measurements or constraints. The measurements range from $< 25\%$ of solar to 81% of solar, with a median of 37% of solar (where solar is from ?.) Several of the MEGaSaURA galaxies have redshifts such that the rest-frame optical oxygen abundance diagnostics are not accessible from the ground; access to these diagnostic lines was not a selection criterion. Oxygen abundances for other SGAS galaxies, not in the MEGaSaURA sample, were published in Wuyts et al. (2012b); the median and quartile ranges are $66^{+27}_{-36}\%$ of solar.

The MEGaSaURA sources are exceptionally bright: the

brightest has $g_{AB} = 19.15$ (Wuyts et al. 2010), and most have $g_{AB} \sim 20\text{--}21$ (Koester et al. 2010; Fig. 5 of Wuyts et al. 2012a). For comparison, individual field galaxies that went into the composite spectrum of Shapley et al. (2003) have $g_{AB} \sim 24.7$ (Erb et al. 2006). The MEGaSaURA targets are many of the brightest lensed sources selected from the Sloan Digital Sky Survey.

Table 1 lists the targets, coordinates, and total integration times. Figure 1 and Figure 2 contain findercharts for the MEGaSaURA sample.

Portions of the MEGaSaURA spectra have been published previously. Koester et al. (2010) published smoothed spectra for SGAS J122651.3+215220 and SGAS J152745.1+065219. Rigby et al. (2014) pointed out the lack of correlation between the Mg II emission and Ly α emission in five of these galaxies. Bayliss et al. (2014) published the MagE spectrum of the highest redshift galaxy in the sample, SGAS J105039.6+001730 at $z = 3.6252$. Rigby et al. (2015) analyzed [C III] 1907, C III] 1909 Å emission for the sample. Bordoloi et al. (2016) analyzed variation in the Mg II and Fe II emission and absorption among four star-forming knots within lensed galaxy RCS-GA 032727–132609.

2.2. Spectroscopic observations

Observations were obtained with The Magellan Echelle (MagE) spectrograph (Marshall et al. 2008) on the twin 6.5 m Magellan telescopes at the Las Campanas Observatory in Chile. The majority of observations were conducted with MagE mounted on the Clay telescope; some observations were made after October 2015, when MagE was moved to the Baade telescope. Targets were acquired by blind offsets from bright nearby stars; target acquisition was verified via the slit-viewing guider camera. MagE has eight available slits, all $10''$ in length. We used slit widths of 0.7, 0.85, 1.0, 1.5, and $2''$, with the slit width chosen to match the atmospheric seeing and the compactness of the emission.

For two galaxies, RCS-GA 032727–132609 and SGAS J152745.1+065219, we obtained spectra of multiple physically distinct regions, as noted in Table 1 and on the findercharts in Figure 1 and Figure 2.

The broad wavelength coverage of MagE makes it important to keep the slit position angle close to the parallactic angle, especially when the airmass is significant (Filippenko 1982). This was done by advancing the slit angle to where the parallactic angle was expected 30 minutes hence, acquiring the object, exposing (typically for one hour), and repeating. A few exceptions to this rule were made to keep contaminating objects out of the slit. The slit position angle and parallactic angle are noted in Table 1.

Because these lensed galaxies are highly spatially extended, and because we maintained the parallactic angle, we generally obtained spectra for only a portion of each lensed galaxy. This spatial coverage is illustrated in Figure 1 and Figure 2, which show the slit position angles obtained for each galaxy in the sample.

We obtained calibrations nightly, following the recommended sequences in the MagE manual. Internal Th-Ar lamps were obtained for wavelength calibration. Xe-flash lamp exposures, using the same slit as the science observations, were obtained to define where the spectral orders

fall on the detector.

The wide wavelength coverage of MagE makes it a challenging instrument to flat-field. Our strategy was to take three kinds of flat-field calibrations: calibrations for the bluest two orders, for the other blue orders, and for the red orders. To obtain a high quality flat-field for the bluest two orders, we obtained a sequence of calibration frames (“very blue flats”) using the internal Xe-flash lamp, long (100 s) integration times, and with the 5” slit and the instrument defocused to blur out the broad Xe emission lines. These frames have good counts in the two bluest two orders, and saturate the others. To calibrate the remaining blue orders, we obtained shorter (10–15 s) Xe-flash exposures (“blue flats”), again with the 5” slit and the instrument defocused. To calibrate the redder orders, we obtained calibration frames (“red flats”) using a quartz lamp mounted in the secondary cage, and the same slit as the science observations.

Nightly we observed spectrophotometric standard stars, chosen from the Nearby Supernova Factory Spectroscopy Standards list.¹⁰

2.3. Spectroscopic pipeline processing

For each night, calibrations were generated and the data were processed using the MagE pipeline, which is part of the Carnegie Python Distribution¹¹. Here we summarize what the pipeline does.

Data frames first were subtracted of their bias levels, using the overscan regions. Second, Th Ar lamp frames were used to define the regions of the chip covered by the spectral orders. The inter-order regions were then interpolated to generate a non-parametric model of the scattered light.

Next, two flat-fields were generated: the blue flat frames and very blue flat frames were masked of their saturated regions and combined using a weighted average, to produce a blue flat, with high signal-to-noise in the blue, but saturated in the red. The red flat frames were combined in the same way to produce a red flat, that is unsaturated in the red, but has low signal-to-noise in the blue. The blue flat and the red flat were then combined by masking out saturated regions, and combining with a weighted average to create a flat field. This flat-field was then used to flat-field the individual spectral exposures.

Individual spectra were then sky subtracted. The sky emission was modeled using routines described in Kelson (2003), but with explicit masking of pixels that are contaminated by the target. The requisite rectification transformations to account for line curvature were derived using routines described in Kelson et al. (2000) that analyze the tracings of cross correlations of image sections in the comparison Th Ar lamp frames.

After sky subtraction, one-dimensional spectra for the objects were extracted using a multi-exposure optimal extraction algorithm¹², in which the spatial profile of the object in each exposure is characterized by a Gauss-Hermite decomposition with moments that are polynomial functions of order number and position across the detector. With the spatial profile of the object characterized in this manner for each exposure, a single univari-

ate B-spline (Dierckx 1983) representation of the object spectrum can be derived that, in a least-squares sense, best represents all of the available data simultaneously.

The output of the pipeline is an extracted, one-dimensional, wavelength-calibrated spectrum for each echelle order.

2.4. Spectroscopic post-pipeline processing

In order to flux the spectra, we computed the sensitivity function for each night using the IRAF¹³ tools **standard** and **sensfunc** in the **noao.onedspec** package. The sensitivity functions for each standard star observation typically show a spread in normalization of up to 20–30% peak-to-peak in the red, and up to 40% in the bluest orders; this is consistent with expected seeing variations, as gauged by the Magellan seeing monitor. We scaled the sensitivity functions to the star with the highest throughput to create a composite sensitivity function. To flux calibrate, these sensitivity functions were applied to each spectrum using the IRAF tool **onedspec.calibrate**.

After fluxing, we combined the overlapping echelle orders, using a weighted average, weighted by the inverse variance, to make a continuous spectrum for each target for each night. Each spectrum was then corrected to vacuum barycentric wavelength. For each galaxy, the spectra from multiple nights were combined with a weighted average, weighted by the inverse variance. For the two galaxies where we obtained spectra of multiple distinct physical regions, as noted in Table 1, we separately combine the spectra of each distinct region.

The output spectra have vacuum barycentric wavelength in Å and flux density f_ν in $\text{erg s}^{-1} \text{cm}^{-2} \text{Hz}^{-1}$.

There are significant telluric absorption features redward of 6400 Å, primarily the A-band of molecular oxygen, which covers 7590 Å to 7660 Å (Wark & Mercer 1965), and the B-band (6860–6890 Å). For observing runs where the featureless standard star EG 131 was observed, we used that star and the IRAF tool **noao.onedspec.telluric** to correct those telluric features in the two spectral orders that are centered at 6730 and 7570 Å.

The brightest night sky lines, [O I] 5577Å and [O I] 6300Å, frequently saturate individual exposures, which results in artifacts at those wavelengths.

The MagE spectrograph is extremely sensitive in the blue, with sensitivity down to 3000 Å. However, the Earth’s atmospheric transmission at 3000 Å is only 0.6%, as compared to 17.7% at 3200 Å and 28.7% at 3400 Å (Cox 2000 Table 11.25.) Based on examination of MagE spectra of spectrophotometric standard stars, we chose not to use spectra from the bluest order of MagE, and not to use spectra < 3200 Å in the next order. Due to detector fringing, the pipeline does not extract the two reddest orders of MagE. Therefore, we extract spectra over the wavelength range 3200 Å to 8280 Å.

The spectra of six MEGA SaURA galaxies have coverage blueward of the Lyman limit at rest-frame 912 Å.

¹⁰ <http://snfactory.lbl.gov/snf/snf-specstars.html>

¹¹ <http://code.obs.carnegiescience.edu>

¹² Described at <http://code.obs.carnegiescience.edu/>

¹³ IRAF is distributed by the National Optical Astronomy Observatory, which is operated by the Association of Universities for Research in Astronomy (AURA) under a cooperative agreement with the National Science Foundation.

We have summed the flat-fielded, sky-subtracted, two-dimensional spectra for each of these galaxies, and note the bluest wavelength where we see the continuum trace; in each case, we see flux down to the Lyman limit, but not blueward. Therefore, we trim the final 1D spectrum of each galaxy at an observed wavelength that is the greater of 3200 Å or $(1+z)912$ Å.

To measure the instrumental line spread function, which determines the spectral resolution, we extract and combine the spectra of the night sky line emission in the same way as the object spectra, using the same weights applied to the object spectra. The only difference is that when combining the sky spectra, the observed wavelengths receive no barycentric correction. From the final sky spectra, we identify isolated, bright night sky emission lines, fit each with a Gaussian, and measure the median resolution over the spectrum, where the resolution $R \equiv \lambda/\delta\lambda$, with $\delta\lambda$ defined as the full width at half maximum. The spectral resolving powers range from $R=2500$ to $R=4700$, with an average of $R = 3300$, and are tabulated in Table 1. For combined spectra taken with the 2'' slit, the median resolution and standard deviation are $R = 2545 \pm 37$; the observations taken with the 1'' slit have $R = 4770 \pm 8$. As expected for an echellette, the spectral resolution is constant with wavelength. These measured resolutions are higher than the design resolution of $R \sim 4100$ for a 1'' slit (Marshall et al. 2008).

We correct the flux density of each spectrum for Milky Way reddening, using the $E(B - V)$ value derived from Pan-STARRS 1 and 2MASS photometry by Green et al. (2015),¹⁴ assuming an extinction-to-reddening constant of $R_v = 3.1$, and the reddening curve of Cardelli et al. (1989). Table 1 lists the $E(B - V)$ values used.

As discussed above, spectra were only obtained for a portion of each lensed galaxy. The fluxing is therefore appropriate for the observed portion of the galaxy. To illustrate this, we use the example of SGAS J122651.3+215220. Koester et al. (2010) improved on the SDSS DR7 photometry through careful subtraction of neighbors, measuring (g,r,i) AB magnitudes of 21.14, 20.60, and 20.51. Using kcorrect (Blanton & Roweis 2007), we measure the SDSS AB-magnitudes of the flux-calibrated MagE spectrum to be $g,r,i = 22.15, 21.70, \text{ and } 21.62$. The offset between these measurements implies that the slit captured 39%, 36%, and 36% of the total light in g,r,i from this lensed galaxy.

2.5. Continuum fitting

Continuum fitting is necessarily a somewhat arbitrary process. At the high signal-to-noise and spectral resolution of MEGaSaURA, the problem is compounded because the so-called continuum is not in fact featureless. Rather, it is the sum of the rest-frame ultraviolet spectra of many hot stars, and as such contains numerous weak photospheric absorption features. Different continua are required for different purposes; we have therefore computed several different kinds of continuum fits.

1. Hand-fit smooth continua: We interactively fit splines to the continuum of each galaxy, using the

`x_continuum` tool in the XIDL package. The continuum was fit from spectral regions that are free from expected emission or absorption lines at the galaxy redshift (including Lyman α), intervening absorption lines, or contamination from night sky lines. `x_continuum` also employs iterative sigma rejection to remove spectral features. We exclude from the fit the spectral region within $\lambda_r \pm 30$ Å of C IV 1548, 1551 Å. For each galaxy, we fit the continuum three times, looping over the sample to minimize human error; we then adopt as the continuum the mean of the three fits, and as the uncertainty the error in the mean. This process allows us to quantify the uncertainty due to the subjectivity of manual continuum fitting. The resulting continuum is smooth and has no knowledge of the underlying stellar emission; it is therefore most appropriate for analyzing the velocity profiles of transitions tracing the interstellar medium.

2. Automatic continua: We automatically generate smooth continua as follows. For each spectrum, after masking out bad pixels as well as regions with velocities within 500 km s⁻¹ of known emission and absorption features, we smooth by convolving with a boxcar of width $\lambda_{rest} = 100$ Å. The resulting continuum is smooth and has no knowledge of the underlying stellar emission. Since this continuum is automatically generated, it can be applied to a large number of theoretical models.
3. Stellar continua: We have generated best-fit spectra from linear combinations of Starburst99 models (Leitherer et al. 1999, 2010, 2014), each an instantaneous starburst with a given age (between 1–40 Myr) and stellar continuum metallicity (with metallicities of 0.05, 0.2, 0.4, 1.0, and 2.0 Z_{\odot}), while simultaneously fitting for a stellar extinction ($E(B - V)$) from the line of sight dust reddening using a Calzetti extinction law (Calzetti et al. 2000). This fit is made assuming a linear combination of the 50 stellar continuum models, and fitting for the linear coefficient (the fraction of the total light attributed to each Starburst99 model) using a least-squares method following the methodology of Chisholm et al. (2015). Regions within 500 km s⁻¹ of known emission and absorption features were masked before fitting. We use fully theoretically Starburst99 models that are computed using the Geneva stellar evolution tracks with high mass-loss (Meynet et al. 1994), computed using the WM-BASIC method (Leitherer et al. 2010), and assuming a Kroupa IMF with a high (low) mass power-law index of 2.3 (1.3) with a high-mass cut-off of 100 M_{\odot} . This modeling, and derived constraints on the stellar populations, will be described in a sub-sequent paper (Rigby et al. in prep.) that comprehensively analyzes the diagnostics of hot stars in the MEGaSaURA spectra. What is relevant for the current paper is that these models fit the underlying stellar spectra, and can therefore be used to estimate the redshift of the stars, commonly known as the systemic redshift.

¹⁴ Queried using the API provided by those authors at <http://argonaut.skymaps.info>

2.6. Measurement of redshifts

We measure the redshifts of the stars, the nebulae, and the interstellar medium for each galaxy, as follows.

The stellar redshift is an output from the Starburst99 fitting (Rigby et al. in prep.), in which we cross-correlate the model and the observed data to find the most likely stellar redshift. We shift the Starburst99 models in velocity-space by 10 km s^{-1} increments over a range of $\pm 600 \text{ km s}^{-1}$ from the measured nebular redshift. We then produce a likelihood function by taking the inverse exponential of the χ^2 function using the observed data and the shifted Starburst99 models. We calculate the likelihood at each velocity shift, normalize the likelihood function, and take the expectation value and standard deviation of this probability density function as the best-fit redshift and the redshift uncertainty. As such, the quoted redshift uncertainty does not take into account the full range of possible stellar models.

For 12 of the spectra in the MEGaSaURA sample, the nebular redshift is measured from the [C III] 1907, C III] 1909 \AA doublet, since these are generally the brightest rest-frame UV nebular lines. We determine a redshift for the [C III] 1907, C III] 1909 feature by fitting two Gaussians with a common linewidth, holding fixed the ratio of the central wavelengths, using the IDL Levenberg-Marquardt least-squares fitting code MPFITFUN (Markwardt 2009), following Rigby et al. (2014). The uncertainty quoted is the uncertainty from MPFITFUN.

Table 1 notes that for 5 spectra, the nebular redshift is sourced differently, from nebular lines in the rest-frame optical. While lines like $H\beta$ and [O III] 5007 \AA generally have higher fluxes than [C III] 1907, C III] 1909 \AA , using them may introduce systematic wavelength calibration errors when comparing to stellar redshifts measured from the rest-frame UV continuum.

To test for systematic effects, we measured redshifts individually for [C III], C III], and weaker rest-frame UV emission lines ([O III] 1666, Si III] 1882, Si III] 1892, C II] 2325, and [O II] 2470), in four spectra with high signal-to-noise ratio (RCS0327-knotE, S0004-0103, S0108+0624, and S0957+0509.) We note a systematic effect, that compared to other rest-frame UV emission lines, [C III] 1907 is blueshifted in all cases by up to 40 km s^{-1} , while in three of four cases C III] 1909 is redshifted by up to 20 km s^{-1} . The standard deviation is $10\text{--}20 \text{ km s}^{-1}$. This effect appears to be real; we do not understand its origin. Perhaps the forbidden [C III] 1907 and semi-forbidden C III] 1909 arise in different physical regions with different velocities. Perhaps the line profiles are intrinsically asymmetric, driven by winds, and the bias comes from fitting them with Gaussians. In any case, we mitigate this bias by using both transitions to determine the redshift, as described above.

The interstellar medium redshift is measured as the average redshift of Gaussian fits to C II 1334, Si II 1526, Al II 1670, Al III 1854 and Al III 1862; the uncertainty is the standard deviation. The measured redshifts are tabulated in Table 1.

3. RESULTS

3.1. The MEGaSaURA spectra

Figure 3 shows the per-pixel signal-to-noise ratios (SNR) for the final combined MEGaSaURA spectra. The median per-pixel dispersion is 0.35 \AA in the observed frame. A total of 8 spectra have per-pixel $SNR > 10$ over the observed wavelength range of $5000\text{--}7000 \text{ \AA}$; the median spectrum has a per-pixel $SNR \sim 10$. For the average resolution, at 5000 \AA this corresponds to $SNR = 21$ per resolution element.

The final combined MEGaSaURA spectra are plotted in Figure 4. The MEGaSaURA spectra comprise a spectral atlas at “cosmic noon” that has superior signal-to-noise ratio and wavelength coverage, albeit lower spectral resolution, than the COS/*HST* archive of starburst galaxies in the local universe.

3.2. Contribution from Active Galactic Nuclei

Two galaxies in our sample show evidence of active galactic nuclei (AGN). The MagE spectrum of SGAS J224324.2–093508 shows broad emission lines of Lyman α , N V, C IV, and [C III], that together indicate that this galaxy hosts a broad-line AGN. The *HST* imagery (Figure 1) shows a spatially extended host galaxy with a central point source. The MagE spectrum of SGAS J003341.5+024217 does not show obvious AGN diagnostics. However, a VLT/SINFONI observation shows that the nucleus exhibits high-ionization [O III] 5007 / $H\beta$ and $H\alpha$ /[N II] ratios, and also broad wings in $H\alpha$ (E. Wuyts, private communication.) It is thus implicated as having a weak AGN.

3.3. Velocity offsets

Figure 5 compares the velocity offsets among the interstellar medium, stars, and nebulae of the MEGaSaURA spectra, measured as described in § 2.6, and tabulated in Table 1. The top left panel of Figure 5 shows that there is no systematic offset between the redshifts of the hot stars and the nebulae; the median offset and median absolute deviation are $-1 \pm 31 \text{ km s}^{-1}$; from bootstrapping, the 80% confidence interval on the median is $-1_{-11}^{+20} \text{ km s}^{-1}$.

The top right panel of Figure 5 shows that the ISM lines are systematically blue-shifted with respect to the stellar continuum, with a median offset and median absolute deviation of $-148 \pm 35 \text{ km s}^{-1}$, and bootstrapped 80% confidence interval on the median of $-148_{-11}^{+42} \text{ km s}^{-1}$. This is to be expected given the ubiquity of galaxy-wide winds in $z \sim 2$ galaxies (Shapley et al. 2003; Weiner et al. 2009; Rubin et al. 2014).

We now place these measurements in a larger context. Because purely stellar features like the photospheric absorption lines are only detectable with high signal-to-noise and moderate spectral resolution, it is common practice in the literature to use nebular emission lines as a proxy for the systemic redshift. Doing so makes two assumptions—that the ionized gas is well-mixed with the hot stars, and that outflows do not seriously bias the nebular line redshifts. The local galaxy NGC 7552 shows that such biases can occur: $H\alpha$ is blueshifted from the stellar redshift by -30 km s^{-1} due to a wind, but this blueshift is much less than the bulk outflow velocity as traced by rest-frame UV absorption lines. These assumptions are testable for the MEGaSaURA spectra. In §2.6 we reported that the brightest emission lines in the rest-frame UV, [C III] 1907 and C III] 1909 \AA , may be

systematically biased by up to 40 km s⁻¹ with respect to each other, and with respect to still weaker rest-frame UV lines. Since one line is systematically blue-shifted and the other red-shifted, we attempted to mitigate the bias by jointly fitting the [C III], C III] doublet. Indeed, the median offset between the nebular redshifts and systemic redshifts, -1_{-11}^{+20} km s⁻¹ (80% confidence) is fully consistent with no offset. This is consistent with the measurement of Shapley et al. (2003) for their stack of Lyman Break Galaxies: -10 ± 35 km s⁻¹.

We conclude that while nebular redshifts can be used as proxies for systemic redshifts, one should be aware of systematic biases at the level of tens of km s⁻¹ when using only one line of the [C III], C III] doublet. In the era of the *James Webb Space Telescope (JWST)*, such biases may limit kinematic studies. The stellar redshifts we measure, by fitting the whole stellar continuum, should be unbiased to outflows, but are less precise than the nebular redshifts (median fractional uncertainty of 3×10^{-4} , versus 4×10^{-5}). Greater precision can be obtained by fitting individual photospheric absorption lines, when they are clearly detected. This is the case for about half the MEGaSAURA spectra, and will be explored in a future paper.

4. SUMMARY

In this Paper, we introduce Project MEGaSAURA: The Magellan Evolution of Galaxies Spectroscopic and Ultraviolet Reference Atlas. This is the sample and data release paper for that project, in which we present high-quality, medium-spectral resolution rest-frame ultraviolet spectra for $N = 15$ lensed galaxies. Given the wealth of spectral diagnostics in the $1000 < \lambda_r < 3000$ Å spectral region covered by these spectra, the MEGaSAURA spectra should enable a number of investigations into the nature of star-forming galaxies at cosmic noon.

Using the measured redshifts for the stars, the nebulae, and the interstellar medium in these galaxies, we analyze the relative velocity offsets. Relative to the stars, the ISM gas shows an expected bulk outflow of -148 ± 35 km s⁻¹ (median and median absolute deviation). We see no offset between the stars and the nebular emission lines: -1 ± 31 km s⁻¹ (median and median absolute deviation). We plan a future paper to analyze the multiphase outflowing winds and the ionized nebulae at $z \sim 2$ as probed by the MEGaSAURA spectra, and compare to galaxies in the local universe.

We have obtained the high-quality MEGaSAURA spectra with an eye toward the future. The $1000 < \lambda_r < 3000$ Å spectral region is unusually rich in spectral diagnostics. This spectral region is what 20–30 m telescopes now under construction will probe for unlensed field galaxies at $z \sim 2$; it is also the spectral region that the James Webb Space Telescope will probe for the galaxies in the epoch of reionization. Given this future, and as a service to the community, we publish electronic versions of the MEGaSAURA spectra.

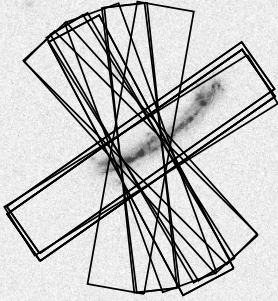
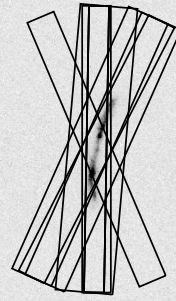
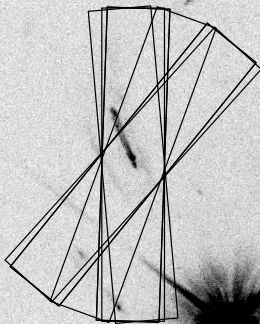
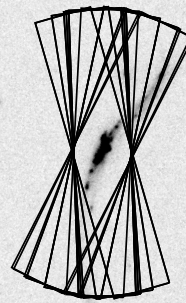
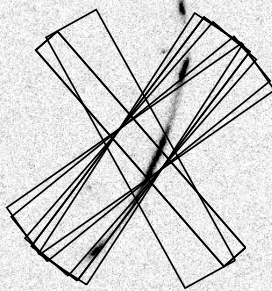
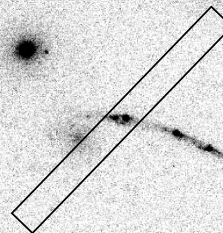
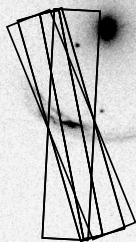
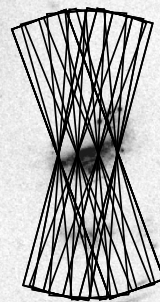
Acknowledgments: This paper includes data gathered with the 6.5 meter Magellan Telescopes located at Las Campanas Observatory, Chile. We thank the staff of Las Campanas for their dedicated service, which has made

possible these observations. We thank the telescope allocation committees of the Carnegie Observatories, The University of Chicago, The University of Michigan, and Harvard University, for supporting this observing program over several years. This paper includes data from observations made with the Nordic Optical Telescope, operated by the Nordic Optical Telescope Scientific Association at the Observatorio del Roque de los Muchachos, La Palma, Spain, of the Instituto de Astrofísica de Canarias.

REFERENCES

- Bayliss, M. B. 2012, *ApJ*, 744, 156
 Bayliss, M. B., Hennawi, J. F., Gladders, M. D., Koester, B. P., Sharon, K., Dahle, H., & Oguri, M. 2011, *The Astrophysical Journal Supplement*, 193, 8
 Bayliss, M. B., Rigby, J. R., Sharon, K., Wuyts, E., Florian, M., Gladders, M. D., Johnson, T., & Oguri, M. 2014, *ApJ*, 790, 144
 Belokurov, V., Evans, N. W., Moiseev, A., King, L. J., Hewett, P. C., Pettini, M., Wyrzykowski, L., McMahon, R. G., Smith, M. C., Gilmore, G., Sánchez, S. F., Udalski, A., Koposov, S., Zucker, D. B., & Walcher, C. J. 2007, *ApJ*, 671, L9
 Bian, F., Fan, X., Bechtold, J., McGreer, I. D., Just, D. W., Sand, D. J., Green, R. F., Thompson, D., Peng, C. Y., Seifert, W., Ageorges, N., Juette, M., Knierim, V., & Buschkamp, P. 2010, *ApJ*, 725, 1877
 Blanton, M. R. & Roweis, S. 2007, *The Astronomical Journal*, 133, 734
 Bordoloi, R., Rigby, J. R., Tumlinson, J., Bayliss, M. B., Sharon, K., Gladders, M. G., & Wuyts, E. 2016, *Monthly Notices of the Royal Astronomical Society*, 458, 1891
 Cabanac, R. A., Valls-Gabaud, D., & Lidman, C. 2008, *Monthly Notices of the Royal Astronomical Society*, 386, 2065
 Calzetti, D., Armus, L., Bohlin, R. C., Kinney, A. L., Koornneef, J., & Storchi-Bergmann, T. 2000, *ApJ*, 533, 682
 Cardelli, J. A., Clayton, G. C., & Mathis, J. S. 1989, *ApJ*, 345, 245
 Chisholm, J., Tremonti, C. A., Leitherer, C., Chen, Y., Wofford, A., & Lundgren, B. 2015, *ApJ*, 811, 149
 Cox, A. N. 2000, *Allen's astrophysical quantities*
 Dessauges-Zavadsky, M., D'odorico, S., Christensen, L., Schaerer, D., & Richard, J. 2011, *Astronomische Nachrichten*, 332, 307
 Diehl, H. T., Allam, S. S., Annis, J., Buckley-Geer, E. J., Frieman, J. A., Kubik, D., Kubo, J. M., Lin, H., Tucker, D., & West, A. 2009, *ApJ*, 707, 686
 Dierckx, P. 1983, *Journal of Computational Physics*, 52, 163
 Erb, D. K., Pettini, M., Shapley, A. E., Steidel, C. C., Law, D. R., & Reddy, N. A. 2010, *ApJ*, 719, 1168
 Erb, D. K., Steidel, C. C., Shapley, A. E., Pettini, M., Reddy, N. A., & Adelberger, K. L. 2006, *ApJ*, 646, 107
 Filippenko, A. V. 1982, *Publications of the Astronomical Society of the Pacific*, 94, 715
 Gilbank, D. G., Gladders, M. D., Yee, H. K. C., & Hsieh, B. C. 2011, *The Astronomical Journal*, 141, 94
 Gralla, M. B., Sharon, K., Gladders, M. D., Marrone, D. P., Barrientos, L. F., Bayliss, M., Bonamente, M., Bulbul, E., Carlstrom, J. E., Culverhouse, T., Gilbank, D. G., Greer, C., Hasler, N., Hawkins, D., Hennessy, R., Joy, M., Koester, B., Lamb, J., Leitch, E., Miller, A., Mroczkowski, T., Muchovej, S., Oguri, M., Plagge, T., Pryke, C., & Woody, D. 2011, *ApJ*, 737, 74
 Green, G. M., Schlafly, E. F., Finkbeiner, D. P., Rix, H.-W., Martin, N., Burgett, W., Draper, P. W., Flewelling, H., Hodapp, K., Kaiser, N., Kudritzki, R.-P., Magnier, E., Metcalfe, N., Price, P., Tonry, J., & Wainscoat, R. 2015, *ApJ*, 810, 25
 Hainline, K. N., Shapley, A. E., Kornei, K. A., Pettini, M., Buckley-Geer, E., Allam, S. S., & Tucker, D. L. 2009, *ApJ*, 701, 52
 Heckman, T. M., Armus, L., & Miley, G. K. 1990, *The Astrophysical Journal Supplement Series*, 74, 833
 Heckman, T. M., Lehnert, M. D., Strickland, D. K., & Armus, L. 2000, *The Astrophysical Journal Supplement Series*, 129, 493
 Hennawi, J. F., Gladders, M. D., Oguri, M., Dalal, N., Koester, B., Natarajan, P., Strauss, M. A., Inada, N., Kayo, I., Lin, H., Lampeitl, H., Annis, J., Bahcall, N. A., & Schneider, D. P. 2008, *The Astronomical Journal*, 135, 664
 Jones, T., Stark, D. P., & Ellis, R. S. 2012, *ApJ*, 751, 51
 Kelson, D. D. 2003, *The Publications of the Astronomical Society of the Pacific*, 115, 688
 Kelson, D. D., Illingworth, G. D., van Dokkum, P. G., & Franx, M. 2000, *ApJ*, 531, 159
 Kewley, L. J. & Ellison, S. L. 2008, *ApJ*, 681, 1183

- Koester, B. P., Gladders, M. D., Hennawi, J. F., Sharon, K., Wuyts, E., Rigby, J. R., Bayliss, M. B., & Dahle, H. 2010, *The Astrophysical Journal Letters*, 723, L73
- Leitherer, C., Ekstrom, S., Meynet, G., Schaerer, D., Agienko, K. B., & Levesque, E. M. 2014, *The Astrophysical Journal Supplement Series*, 212, 14
- Leitherer, C., Ortiz Otálvaro, P. A., Bresolin, F., Kudritzki, R.-P., Lo Faro, B., Pauldrach, A. W. A., Pettini, M., & Rix, S. A. 2010, *The Astrophysical Journal Supplement*, 189, 309
- Leitherer, C., Schaerer, D., Goldader, J. D., Delgado, R. M. G., Robert, C., Kune, D. F., de Mello, D. F., Devost, D., & Heckman, T. M. 1999, *The Astrophysical Journal Supplement Series*, 123, 3
- Maiolino, R., Nagao, T., Grazian, A., Cocchia, F., Marconi, A., Mannucci, F., Cimatti, A., Pipino, A., Ballero, S., Calura, F., Chiappini, C., Fontana, A., Granato, G. L., Matteucci, F., Pastorini, G., Pentericci, L., Risaliti, G., Salvati, M., & Silva, L. 2008, *Astronomy and Astrophysics*, 488, 463
- Markwardt, C. B. 2009, *Astronomical Data Analysis Software and Systems XVIII ASP Conference Series*, 411, 251
- Marques-Chaves, R., Perez-Fournon, I., Shu, Y., Martínez-Navajas, P. I., Bolton, A. S., Kochanek, C. S., Oguri, M., Zheng, Z., Mao, S., Montero-Dorta, A. D., Cornachione, M. A., & Brownstein, J. R. 2017, *ApJ*, 834, L18
- Marshall, J. L., Burles, S., Thompson, I. B., Sheckman, S. A., Bigelow, B. C., Burley, G., Birk, C., Estrada, J., Jones, P., Smith, M., Kowal, V., Castillo, J., Storts, R., & Ortiz, G. 2008, *Ground-based and Airborne Instrumentation for Astronomy II*. Edited by McLean, 7014, 169
- Martin, C. L. 2005, *ApJ*, 621, 227
- Meynet, G., Maeder, A., Schaller, G., Schaerer, D., & Charbonnel, C. 1994, *Astronomy and Astrophysics Supplement Series*, 103
- Oguri, M., Bayliss, M. B., Dahle, H., Sharon, K., Gladders, M. D., Natarajan, P., Hennawi, J. F., & Koester, B. P. 2012, *Monthly Notices of the Royal Astronomical Society*, 420, 3213
- Pettini, M. & Pagel, B. E. J. 2004, *Monthly Notices of the Royal Astronomical Society*, 348, L59
- Pettini, M., Rix, S. A., Steidel, C. C., Adelberger, K. L., Hunt, M. P., & Shapley, A. E. 2002, *ApJ*, 569, 742
- Pettini, M., Steidel, C. C., Adelberger, K. L., Dickinson, M., & Giavalisco, M. 2000, *ApJ*, 528, 96
- Pilyugin, L. S. & Thuan, T. X. 2005, *ApJ*, 631, 231
- Quider, A. M., Pettini, M., Shapley, A. E., & Steidel, C. C. 2009, *Monthly Notices of the Royal Astronomical Society*, 1081
- Quider, A. M., Shapley, A. E., Pettini, M., Steidel, C. C., & Stark, D. P. 2010, *Monthly Notices of the Royal Astronomical Society*, 402, 1467
- Rigby, J. R., Bayliss, M. B., Gladders, M. D., Sharon, K., Wuyts, E., & Dahle, H. 2014, *ApJ*, 790, 44
- Rigby, J. R., Bayliss, M. B., Gladders, M. D., Sharon, K., Wuyts, E., Dahle, H., Johnson, T., & Peña-Guerrero, M. 2015, *The Astrophysical Journal Letters*, 814, L6
- Rigby, J. R., Wuyts, E., Gladders, M. D., Sharon, K., & Becker, G. D. 2011, *ApJ*, 732, 59
- Rubin, K. H. R., Prochaska, J. X., Koo, D. C., Phillips, A. C., Martin, C. L., & Winstrom, L. O. 2014, *ApJ*, 794, 156
- Shapley, A. E., Steidel, C. C., Pettini, M., & Adelberger, K. L. 2003, *ApJ*, 588, 65
- Sharon, K., Gladders, M. D., Rigby, J. R., Wuyts, E., Koester, B. P., Bayliss, M. B., & Barrientos, L. F. 2012, *ApJ*, 746, 161
- Skidmore, W., Dell'Antonio, I., Fukugawa, M., Goswami, A., Hao, L., Jewitt, D., Laughlin, G., Steidel, C., Hickson, P., Simard, L., Schöck, M., Treu, T., Cohen, J., Anupama, G. C., Dickinson, M., Harrison, F., Kodama, T., Lu, J. R., Macintosh, B., Malkan, M., Mao, S., Narita, N., Sekiguchi, T., Subramaniam, A., Tanaka, M., Tian, F., A'Hearn, M., Akiyama, M., Ali, B., Aoki, W., Bagchi, M., Barth, A., Bhalerao, V., Bradač, M., Bullock, J., Burgasser, A. J., Chapman, S., Chary, R.-R., Chiba, M., Cooper, M., Cooray, A., Crossfield, I., Currie, T., Das, M., Dewangan, G. C., de Grijs, R., Do, T., Dong, S., Evslin, J., Fang, T., Fang, X., Fassnacht, C., Fletcher, L., Gaidos, E., Gal, R., Ghez, A., Giavalisco, M., Grady, C. A., Greathouse, T., Gogoi, R., Guhathakurta, P., Ho, L., Hasan, P., Herczeg, G. J., Honda, M., Imanishi, M., Inami, H., Iye, M., Kalirai, J., Kamath, U. S., Kane, S., Kashikawa, N., Kasliwal, M., Kasliwal, V., Kirby, E., Konopacky, Q. M., Lépine, S., Li, D., Li, J., Liu, J., Liu, M. C., Lopez-Rodriguez, E., Lotz, J., Lubin, P., Macri, L., Maeda, K., Marchis, F., Marois, C., Marscher, A., Martin, C., Matsuo, T., Max, C., Mcconnachie, A., McGough, S., Melis, C., Meyer, L., Mumma, M., Muto, T., Nagao, T., & Najita, J. R. 2015
- Smail, I., Swinbank, A. M., Richard, J., Ebeling, H., Kneib, J.-P., Edge, A. C., Stark, D., Ellis, R. S., Dye, S., Smith, G. P., & Mullis, C. 2007, *ApJ*, 654, L33
- Stark, D. P., Swinbank, A. M., Ellis, R. S., Dye, S., Smail, I. R., & Richard, J. 2008, *Nature*, 455, 775
- Steidel, C. C., Strom, A. L., Pettini, M., Rudie, G. C., Reddy, N. A., & Trainor, R. F. 2016, eprint arXiv:1605.07186
- Troncoso, P., Maiolino, R., Sommariva, V., Cresci, G., Mannucci, F., Marconi, A., Meneghetti, M., Grazian, A., Cimatti, A., Fontana, A., Nagao, T., & Pentericci, L. 2014, *Astronomy and Astrophysics*, 563, 58
- Veilleux, S., Cecil, G., & Bland-Hawthorn, J. 2005, *Annual Review of Astronomy and Astrophysics*, 43, 769
- Wark, D. Q. & Mercer, D. M. 1965, *Applied Optics* IP, 4, 839
- Weiner, B. J., Coil, A. L., Prochaska, J. X., Newman, J. A., Cooper, M. C., Bundy, K., Conselice, C. J., Dutton, A. A., Faber, S. M., Koo, D. C., Lotz, J. M., Rieke, G. H., & Rubin, K. H. R. 2009, *ApJ*, 692, 187
- Wuyts, E., Barrientos, L. F., Gladders, M. D., Sharon, K., Bayliss, M. B., Carrasco, M., Gilbank, D., Yee, H. K. C., Koester, B. P., & Muñoz, R. 2010, *ApJ*, 724, 1182
- Wuyts, E., Rigby, J. R., Gladders, M. D., Gilbank, D. G., Sharon, K., Gralla, M. B., & Bayliss, M. B. 2012a, *ApJ*, 745, 86
- Wuyts, E., Rigby, J. R., Sharon, K., & Gladders, M. D. 2012b, *ApJ*, 73
- Zhu, G. B., Comparat, J., Kneib, J.-P., Delubac, T. e., Raichoor, A., Dawson, K. S., Newman, J., Y che, C., Zhou, X., & Schneider, D. P. 2015, *ApJ*, 815, 48

SGAS J000451.7-010321**F390W****SGAS J010842.2+062444****F390W****SGAS J003341.5+024217****F555W****SGAS J090003.3+223408****F475W****SGAS J095738.7+050929****F390W****SGAS J105039.6+001730****F606W****Cosmic Horseshoe****F606W****SGAS J122651.3+215220****F606W**

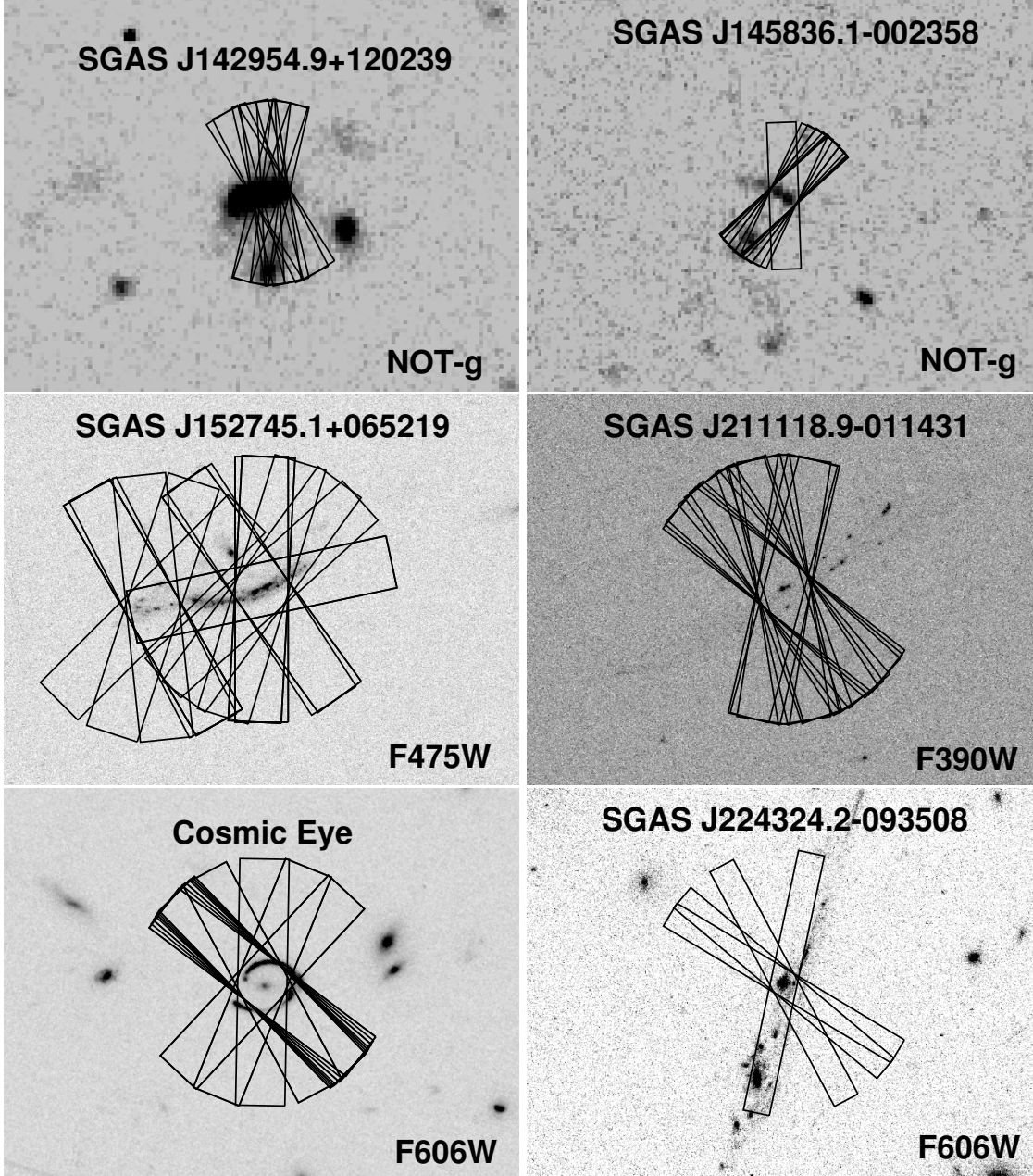


Figure 1. Findercharts indicate what portion of each lensed galaxy was targeted for MagE spectroscopy. RCS-GA 032727–132609 is plotted separately in Figure 2. The filter of the background image used is indicated by text at the lower right of each image: F—W indicates an *HST* image, generally the WFC3 instrument; NOT-g indicates a g-band image from the Nordic Optical Telescope; A slit is drawn for each integration, using our best estimate of where that observation was pointed, as well as the actual slit position angle and slit width. The length of the MagE slit is $10''$. For all images, N is up and E is left.

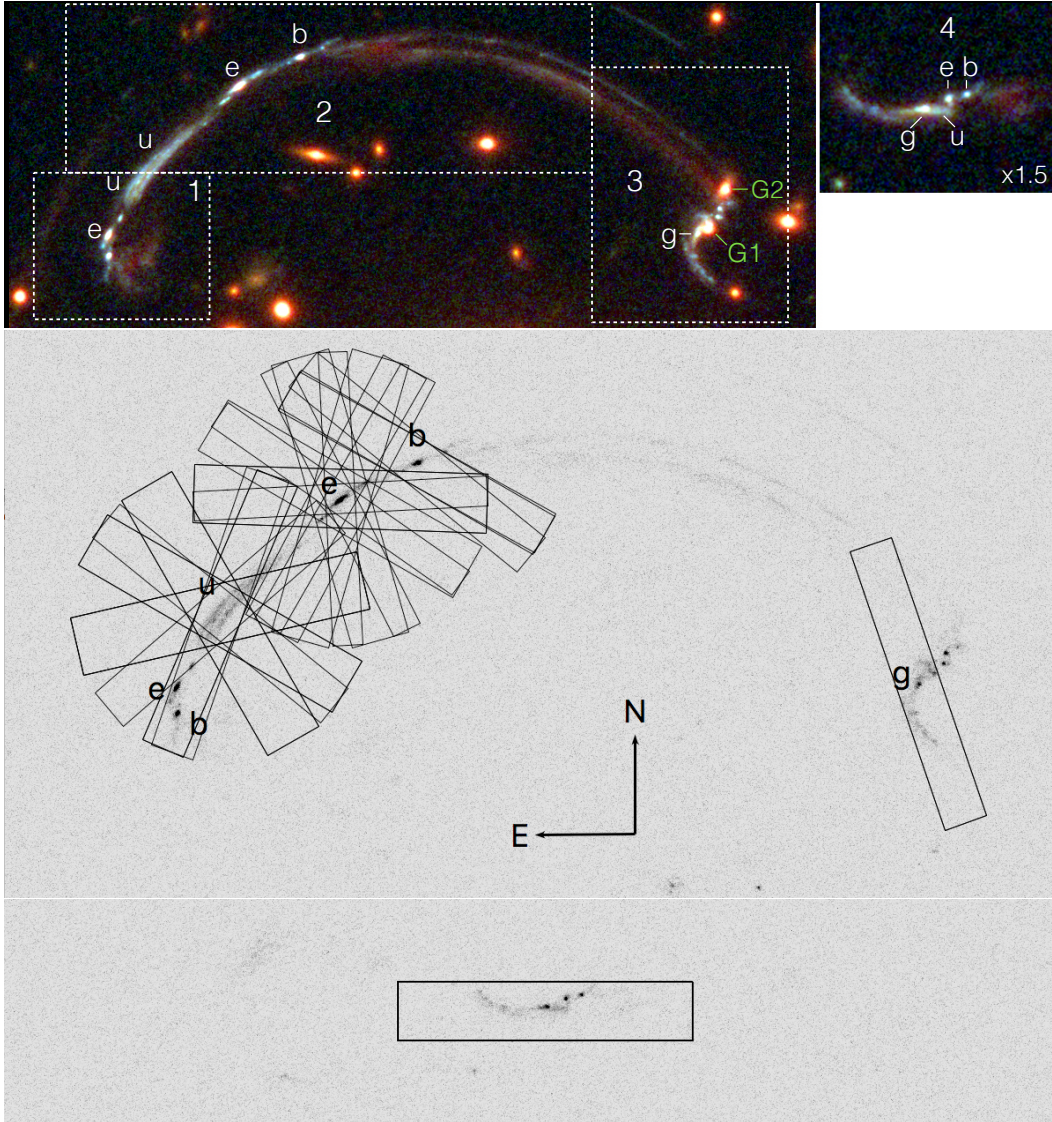
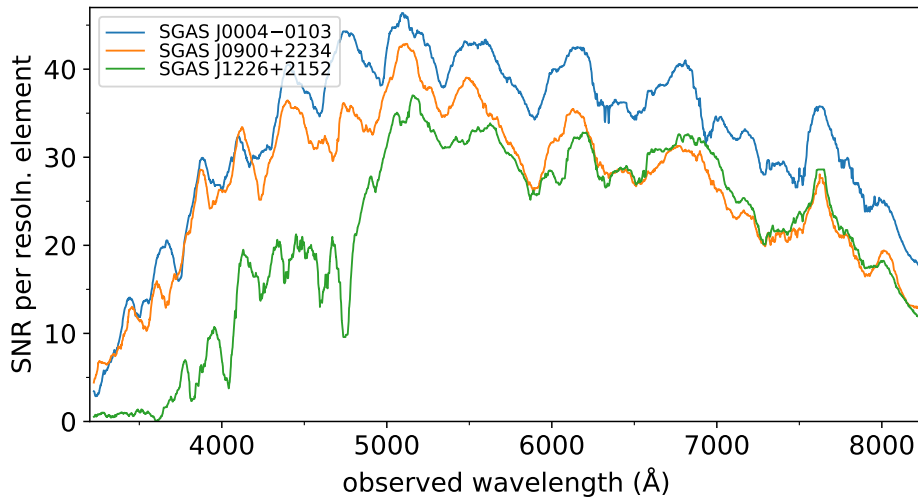
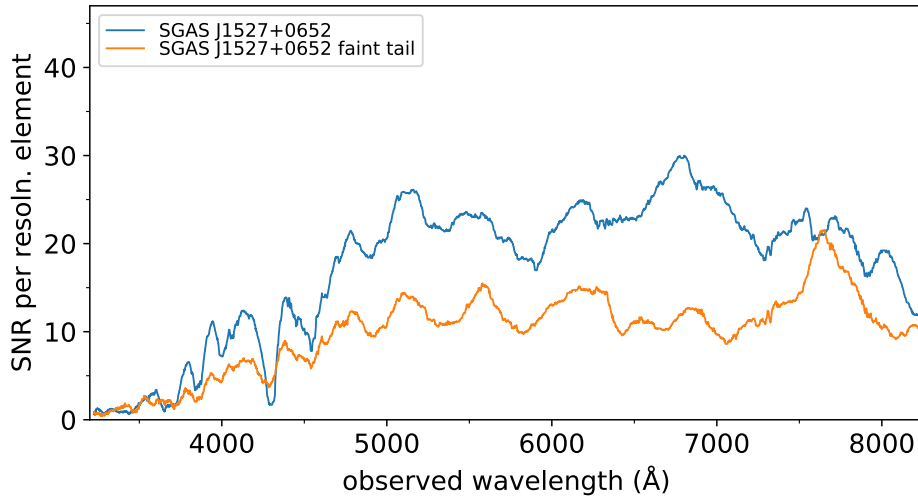
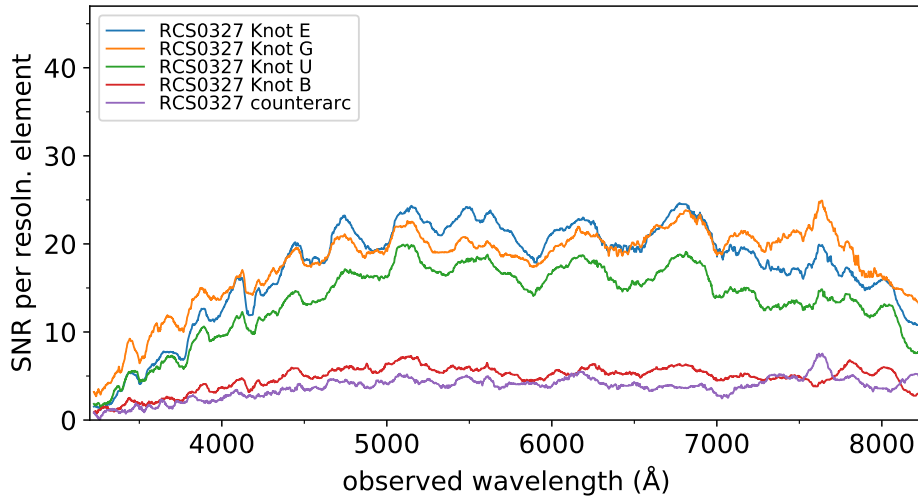


Figure 2. Finderchart for the multiply imaged lensed galaxy RCSGA 032727-132609. TOP PANEL: Color rendition composed of HST/WFC3 F160W, F125W, F098M (red); F814W, F606W (green); and F390W (blue). The dashed lines approximately mark the multiple images, indicated by numbers. The emission knots with MagE spectroscopy are labeled as “e”, “u”, “b”, and “g”, following the labeling of Sharon et al. (2012). Two cluster galaxies “G1” and “G2” interrupt image 3. The right panel shows a zoomed-in (by a factor of $\times 1.5$) view of the counter-image, which is a relatively undistorted image of the source-plane galaxy. Figure adapted from Sharon et al. (2012). MIDDLE AND BOTTOM PANELS: HST/WFC3 F390W image, with MagE observations overlotted. One slit is drawn for each integration, using our best estimate of the pointing, the actual slit position angle, and the slit width used during that observation. Since the slit was regularly rotated to track the parallactic angle, knots U and E were observed using a wide range of slit position angles. The length of the MagE slit is a fixed $10''$. North is up and East is left.



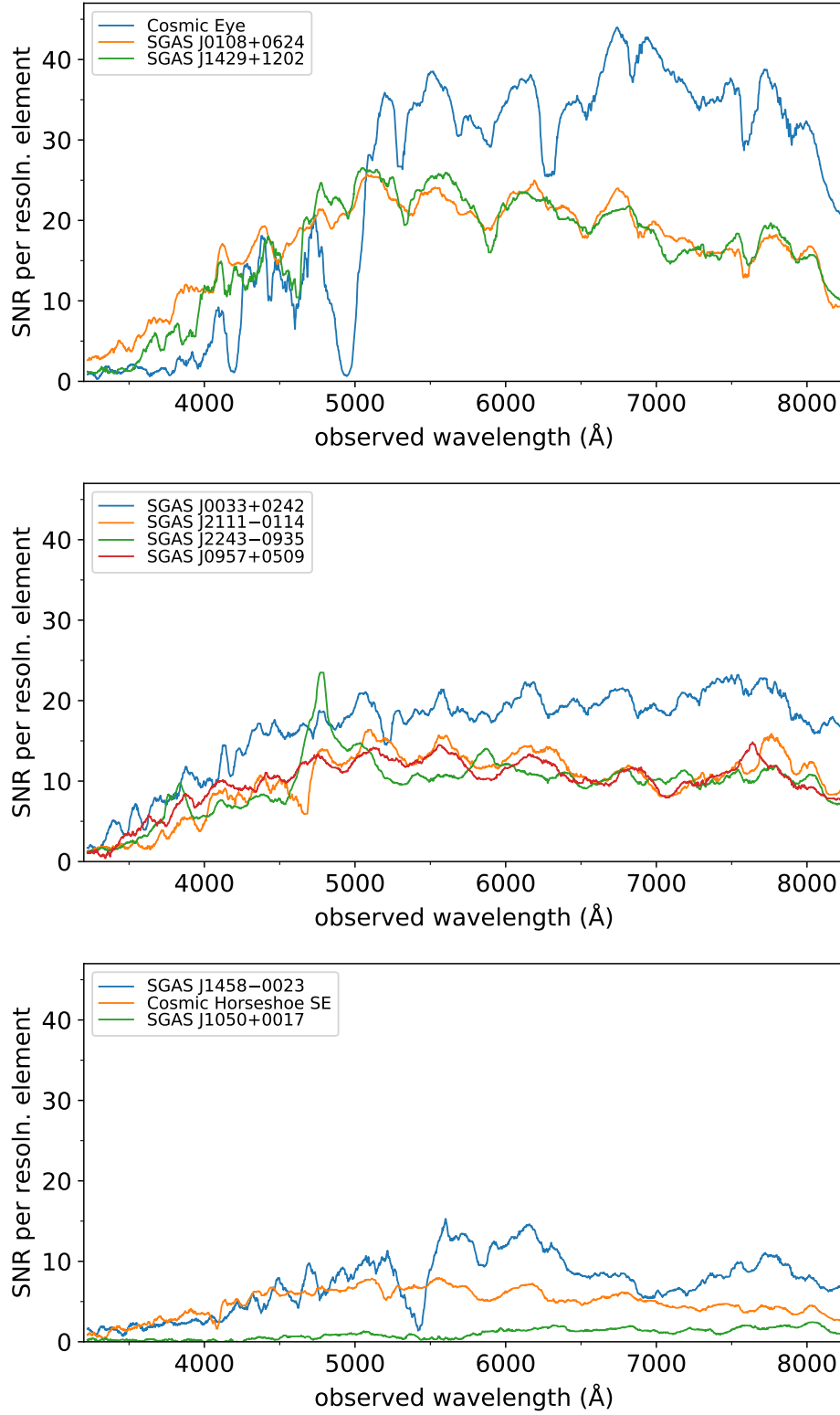
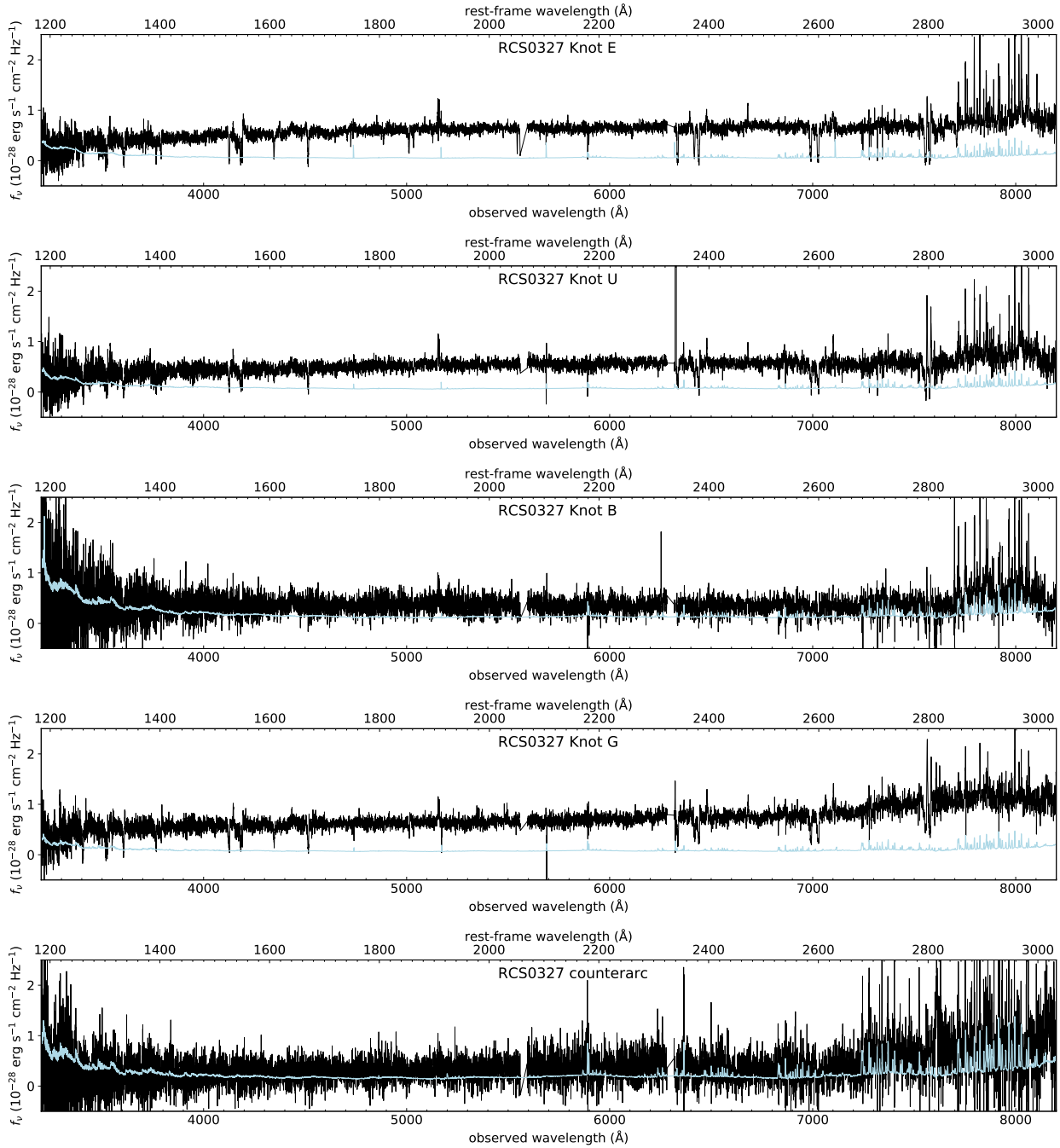
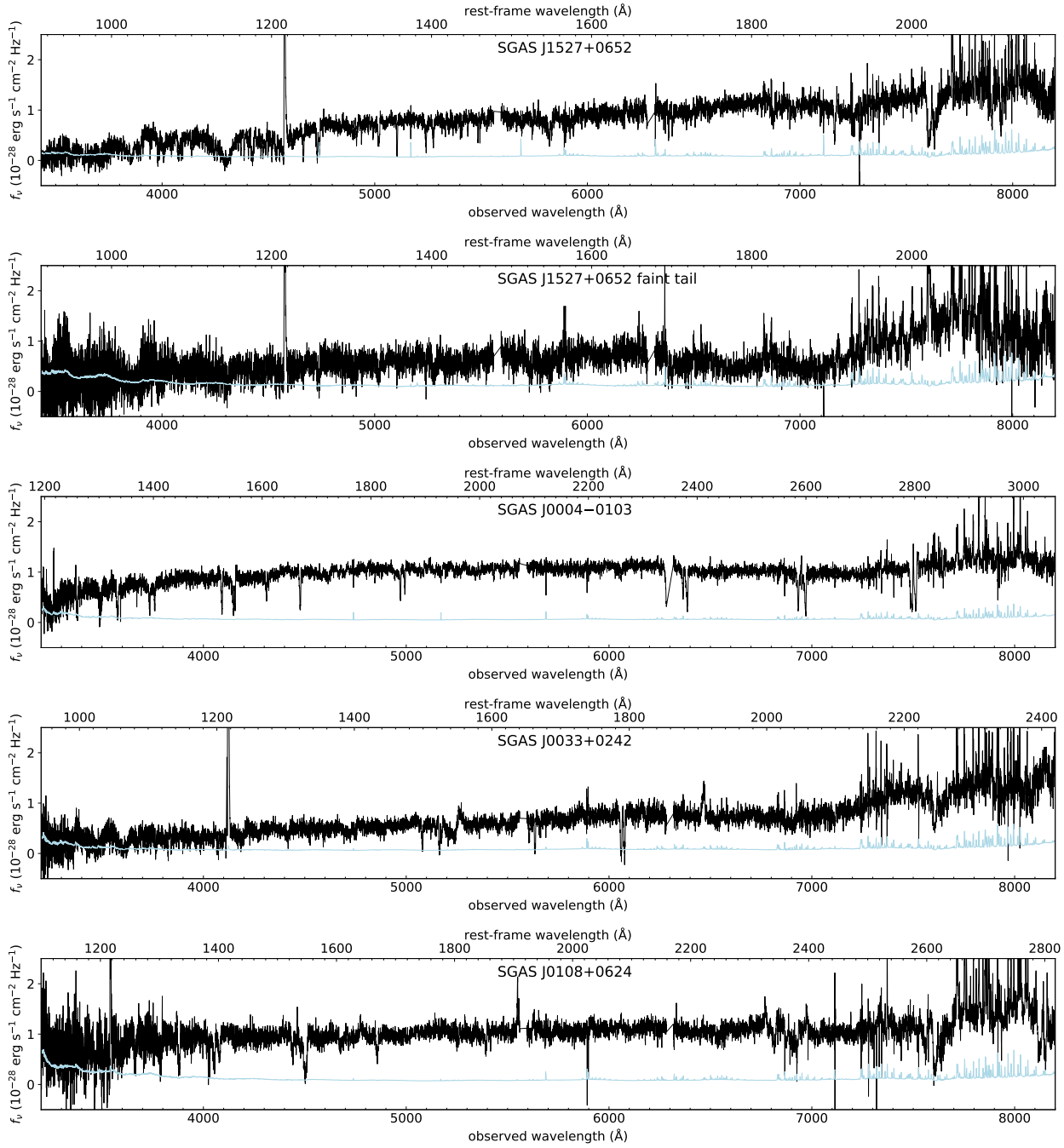
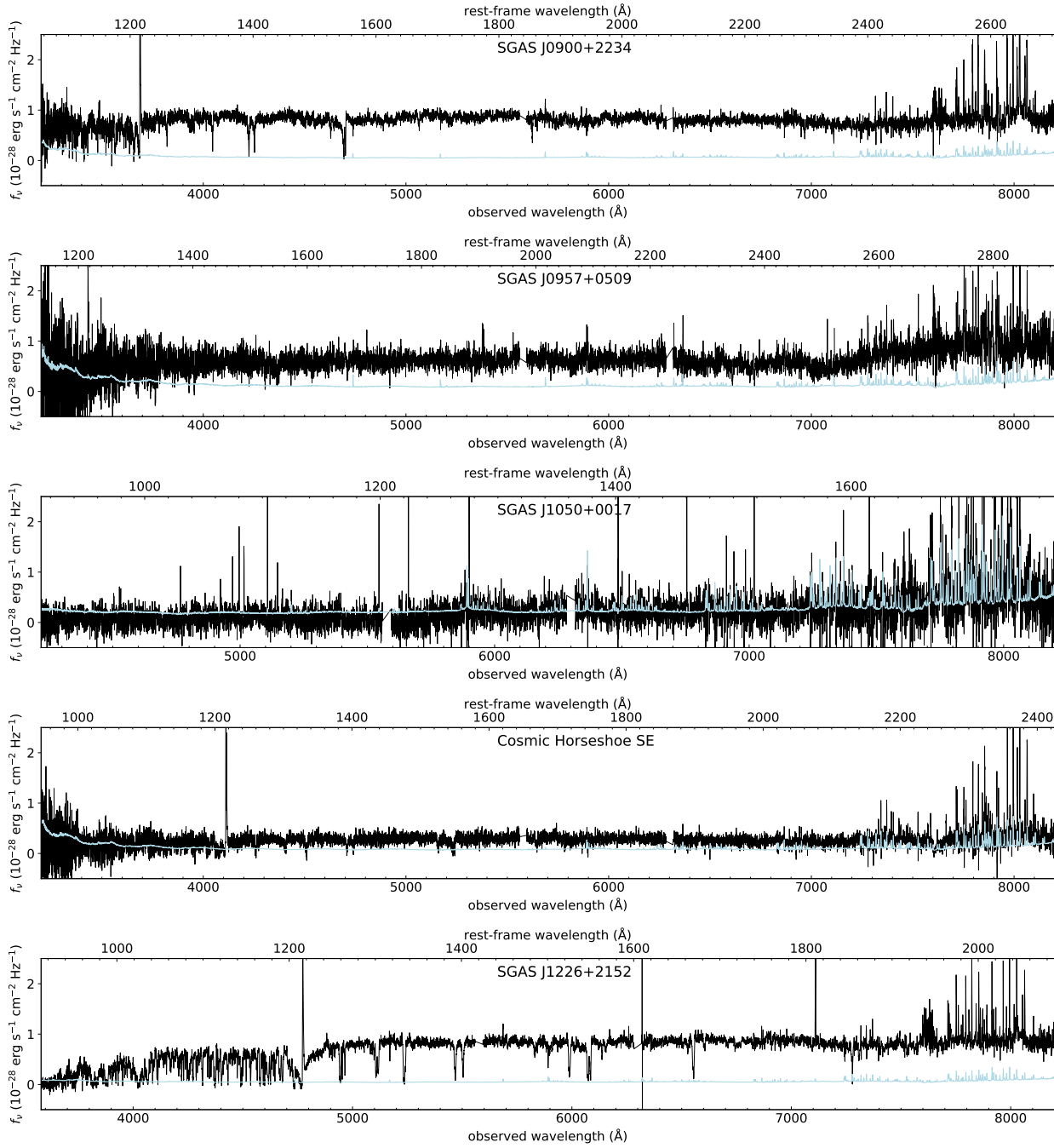


Figure 3. Signal-to-noise ratio of the spectra. For each spectrum, we plot the signal-to-noise per resolution element, smoothed for readability, versus observed wavelength. We plot in separate panels the two galaxies, RCS-GA 032727–132609 and SGAS J152745.1+065219, that have spectra of multiple physical regions. The other galaxies are plotted in order of decreasing signal-to-noise ratio.







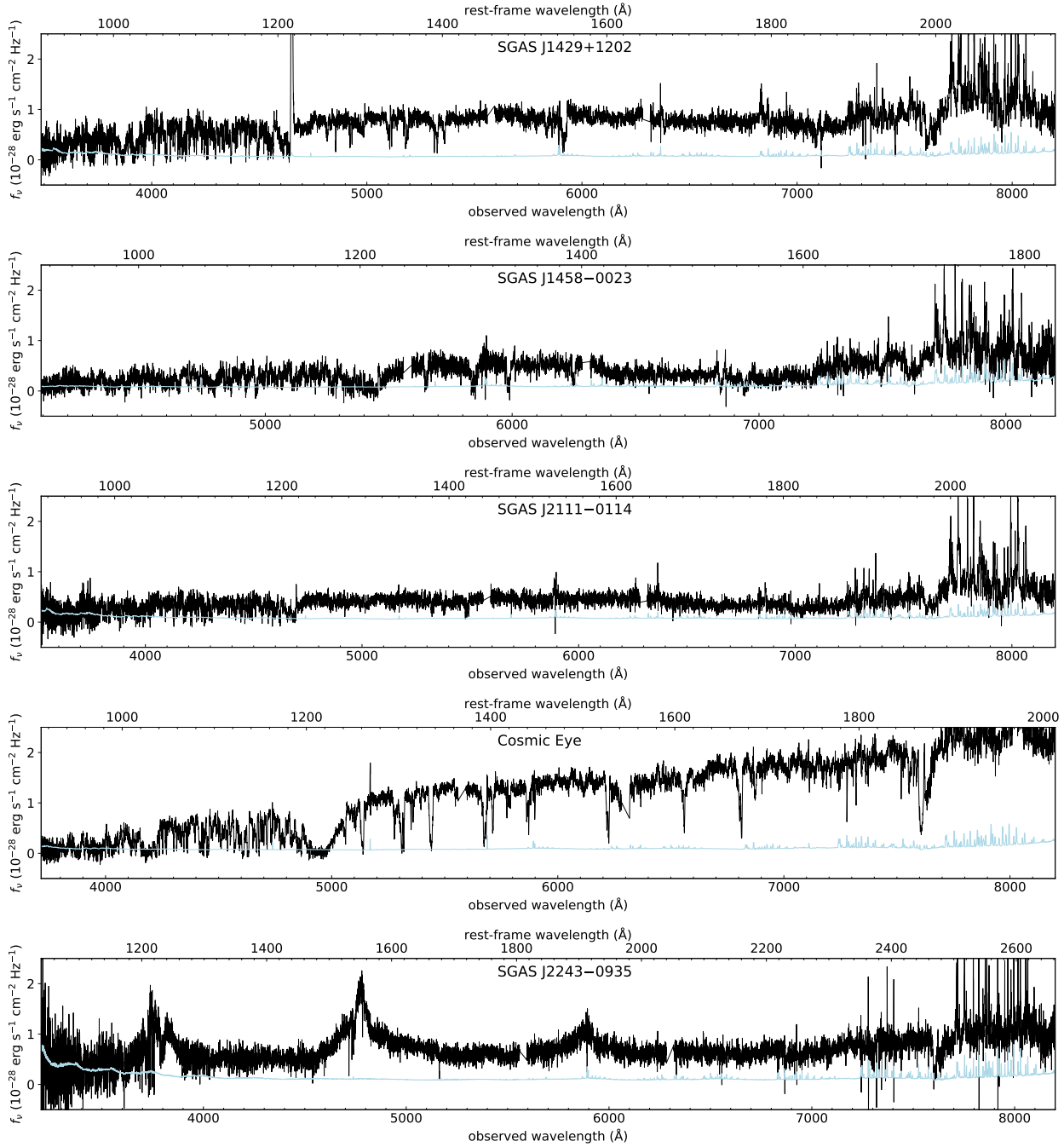


Figure 4. The spectra, and their associated 1σ uncertainty spectra. Wavelengths are in vacuum, are barycentric-corrected, and are in units of \AA ; the lower x-axis shows observed-frame wavelength, and the upper x-axis shows rest-frame wavelength. We have masked the bright sky lines at 5577\AA and 6300\AA . Flux densities (f_ν) are in the observed frame, in units of $\text{erg s}^{-1} \text{ cm}^{-2} \text{ Hz}^{-1}$, and have been corrected for Milky Way reddening.

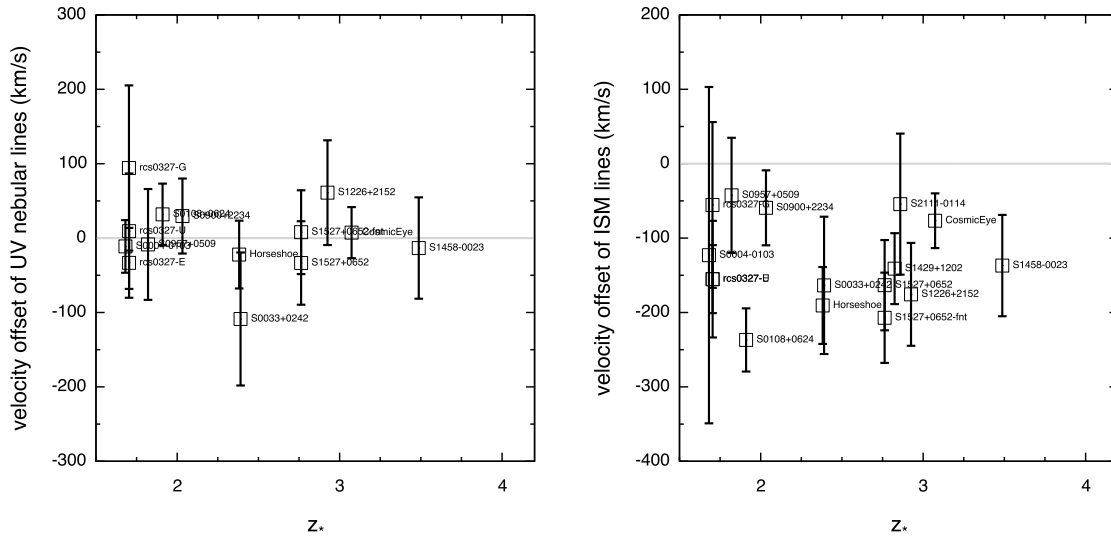


Figure 5. Velocity offsets among the stars, nebular gas, and interstellar medium. The systemic redshift is taken as the stellar redshift z_* , which is measured from Starburst99 fitting to the stellar continuum features including the photospheric absorption lines. The redshift of the ISM lines is measured from the median of Gaussian fits to C II 1334, Si II 1526, Al II 1670, Al III 1854, and Al III 1862 Å absorption lines. The redshift of the nebular lines is measured from fitting the [C III] 1907, [C III] 1909 Å emission line doublet, except as noted in Table 1.

Table 1
The MEGASaURA sample.

Source name	RA (J2000)	DEC (J2000)	t (hr)	R	Galactic E(B-V)	Discovery	References
SGAS J000451.7-010321	00:04:51.685	-01:03:20.86	13.89	2750 ± 100	0.031	SGAS1	Rigby et al. (2014)
SGAS J003341.5+024217	00:33:41.547	+02:42:16.58	7.0	2570 ± 200	0.021	SGAS2	
SGAS J010842.2+062444	01:08:42.206	+06:24:44.41	7.50	4380 ± 200	0.026	SGAS1	Rigby et al. (2014)
RCSGA 032727-132609						Wuyts et al. (2010)	
Knot E	03:27:27.975	-13:26:09.00	10.00	3650 ± 120	0.079		
Knot U	03:27:28.256	-13:26:12.90	7.94	2880 ± 80			
Knot B	03:27:27.796	-13:26:07.76	2.83	3300 ± 100			
Knot G	03:27:26.626	-13:26:15.30	7.33	2830 ± 140			
counterarc	03:27:27.189	-13:26:54.30	1.75	2600 ± 100			
SGAS J090003.3+223408	09:00:03.325	+22:34:07.57	11.00	2530 ± 80	0.031	SGAS1; Diehl et al. (2009)	
SGAS J095738.7+050929	09:57:38.740	+05:09:28.67	6.42	3580 ± 170	0.052	SGAS1	Bayliss et al. (2011)
SGAS J105039.6+001730	10:50:39.575	+0:17:30.13	1.00	4650 ± 230	0.044	SGAS1	Oguri et al. (2012)
Cosmic Horseshoe SE	11:48:33.264	+19:29:59.11	3.89	3980 ± 220	0.047	Belokurov et al. (2007)	
SGAS J122651.3+215220	12:26:51.316	+21:52:20.00	12.42	4010 ± 170	0.021	SGAS1	Koester et al. (2010)
SGAS J142954.9+120239	14:29:54.857	+12:02:38.68	9.25	3500 ± 180	0.032	SGAS2; Marques-Chaves et al. (2017)	
SGAS J145836.1-002358	14:58:36.143	-00:23:58.17	8.00	2500 ± 80	0.059	SGAS2	
SGAS J152745.1+065219					0.032	SGAS1	Hennawi et al. (2008), Koester et al. (2010)
bright	15:27:45.116	+06:52:19.57	8.42	2740 ± 70	0.050		
faint tail	15:27:45.391	+06:52:18.89	5.09	2520 ± 70			
SGAS J211118.9-011431	21:11:18.946	-01:14:31.44	12.11	2650 ± 80	0.084	SGAS1	Hennawi et al. (2008), Gralla et al. (2011)
Cosmic Eye	21:35:12.7	-01:01:42.9	9.11	2530 ± 75	0.0475	Smal et al. (2007)	
SGAS J224324.2-093508	22:43:24.221	-09:35:08.55	4.00	4760 ± 200	0.048	SGAS1	Bayliss et al. (2011)

Note. — Columns: 1) Source name. 2) and 3): Right ascension and declination (J2000) for the center of the MagE slit. Astrometry for most targets is from *HST* images; the exceptions are SGAS J142954.9+120239 and SGAS J145836.1-002358 where the astrometry is from the Nordic Optical Telescope (NOT) images corrected to the USNO system, and SGAS J003341.5+024217 where the astrometry is from IMACS/Magellan images corrected to the USNO system. 4): Total MagE/Magellan on-source integration time. 5): MagE spectral resolution, defined as $R \equiv \lambda/(FWHM)$, where FWHM is the full width at half maximum, measured as the median (\pm the median absolute deviation) of measurements of isolated night-sky emission lines in each combined spectrum. 6) E(B-V) reddening due to the Milky Way Galaxy, from Green et al. (2015). 6): Discovery paper(s) for the arc. We list multiple discovery papers where the arc was independently found by multiple searches. 7) References: Additional references.

Table 2
Oxygen abundances for the MEGASaURA sample.

object	$\log([NII]/H\alpha)$	$12 + \log(O/H)$	method	notes	reference
SGAS J000451.7-010321	< -1.4	< 8.09	Pettini & Pagel (2004) linear		see Note below
SGAS J003341.5+024217					
SGAS J010842.2+062444					
RCSGA 032727-132609	-1.19 ± 0.07	8.22 ± 0.04	Pettini & Pagel (2004) linear	weighted average of 2 measurements	Rigby et al. (2011)
SGAS J090003.3+223408		8.18 ± 0.14	Pettini & Pagel (2004) linear		Bian et al. (2010)
SGAS J095738.7+050929					
SGAS J105039.6+001730		8.3 ± 0.1	multiple R_{23} methods	their ‘‘Aperture 2’’	Bayliss et al. (2014)
Cosmic Horseshoe SE	-0.79 ± 0.04	8.45 ± 0.03	Pettini & Pagel (2004) linear		Hainline et al. (2009)
SGAS J122651.3+215220					
SGAS J142954.9+120239					
SGAS J145836.1-002358					
SGAS J152745.1+065219					
SGAS J211118.9-011431	< -0.65	< 8.5	Pettini & Pagel (2004)		Wuyts et al. (2012a)
Cosmic Eye					
		8.6	R_{23} , Pettini & Pagel (2004); Pilyugin & Thuan (2005)	assumed upper branch	Stark et al. (2008)
		$7.97^{+0.32}_{-0.23}$	Maiolino et al. (2008)		Troncoso et al. (2014)
SGAS J224324.2-093508					

Note. — Compilation of measured oxygen abundances for the MEGASaURA galaxies. We list the measured $\log([NII]/6583/H\alpha)$ ratio, and the resulting inferred oxygen abundance (commonly called the ‘‘metallicity’’) in the format $12 + \log(O/H)$. The measurement for SGAS J0004 is from unpublished FIRE/Magellan spectra, obtained UT 2010-10-14 and UT 2013-09-13, with a total integration time of 4.18 hr.

Table 3
Observation log.

UT Date	UT Time	t_{int} (s)	sec(z)	slit width (")	slit angle (°)	par. angle (°)
SGAS J000451.7-010321						
2010-12-09	00:48:47	1800	1.189	2.0	125	150
2010-12-09	01:19:26	1800	1.254	2.0	125	141
2013-08-10	05:16:34	3600	1.360	2.0	222	226
2013-08-10	06:23:21	3600	1.184	2.0	200	209
2013-08-10	07:28:20	3000	1.132	2.0	170	182
2013-10-06	02:03:58	3400	1.258	1.5	212	219
2013-10-06	03:04:36	3400	1.152	1.5	187	200
2013-10-07	01:08:30	3200	1.450	1.5	225	229
2013-10-07	02:06:07	3200	1.242	1.5	210	218
2013-10-07	03:02:59	3200	1.150	1.5	186	199
2015-11-06	00:54:30	1800	1.163	2.0	302	204
2015-11-06	01:42:00	1800	1.132	2.0	125	183
2015-11-06	02:12:47	3600	1.139	2.0	125	169
2015-11-06	03:13:28	3600	1.215	2.0	125	146
2015-11-06	04:14:17	3600	1.408	2.0	125	132
2015-11-07	00:15:51	2702	1.220	2.0	208	215
2015-11-07	01:01:38	2700	1.151	2.0	208	199
SGAS J003341.5+024217						
2015-11-07	01:50:28	3600	1.181	2.0	178	189
2015-11-07	02:51:13	3600	1.193	2.0	178	165
2015-11-07	03:54:35	3600	1.306	2.0	138	144
2015-11-10	00:17:12	3600	1.311	2.0	180	216
2015-11-10	01:21:19	3600	1.193	2.0	185	196
2015-11-10	02:23:34	3600	1.181	2.0	160	171
2015-11-10	03:29:44	1800	1.273	2.0	141	148
2015-11-10	04:00:49	1800	1.364	2.0	141	140
SGAS J010842.2+062444						
2012-08-19	06:29:45	3600	1.334	1.0	203	210
2012-08-19	07:32:33	3600	1.236	1.0	180	190
2012-08-19	08:41:48	3600	1.250	1.0	156	165
2012-08-20	08:48:26	3600	1.263	1.0	153	161
2012-09-14	07:40:24	2400	1.319	0.7	179	152
2012-09-14	08:21:06	2400	1.449	0.7	179	142
2012-09-14	09:01:34	2100	1.668	0.7	179	134
2013-08-10	08:26:59	2700	1.23	2.0	175	184
2013-08-10	09:15:50	3000	1.25	2.0	156	165
RCSGA 032727-132609 knot E						
2008-07-31	09:03:00	1800	1.268	2.0	240	240
2010-12-09	02:18:04	2700	1.053	2.0	196	210
2010-12-09	03:09:56	3600	1.039	2.0	164	172
2010-12-09	04:20:47	3600	1.099	2.0	152	133
2010-12-09	05:29:20	3600	1.271	2.0	88	120
2010-12-09	06:30:52	2700	1.601	2.0	88	117
2010-12-10	00:48:00	3600	1.198	1.0	235	237
2010-12-10	01:59:40	3600	1.066	1.0	207	218
2010-12-10	03:08:19	3600	1.040	1.0	183	170
2010-12-10	04:26:51	3600	1.116	1.0	150	130
2010-12-10	05:32:13	3600	1.297	1.0	93	120
RCSGA 032727-132609 knot U						
2008-07-31	09:34:55	1800	1.171	2.0	240	236
2008-07-31	10:05:46	900	1.107	2.0	240	229
2010-02-16	00:39:22	1800	1.213	2.0	30	122
2010-02-16	01:10:14	1800	1.323	2.0	30	119
2010-02-17	00:49:53	1800	1.260	2.0	103	121
2010-02-17	01:24:22	1800	1.409	2.0	103	118
2010-02-17	01:55:04	1800	1.604	2.0	103	117
2013-10-06	05:07:01	3300	1.185	1.5	231	236
2013-10-06	06:07:41	3300	1.073	1.5	157	220
2013-10-06	07:06:41	3300	1.038	1.5	157	183
2013-10-07	07:04:20	3500	1.038	1.5	161	182
2013-10-07	08:06:37	3500	1.071	1.5	131	141
RCSGA 032727-132609 knot B						
2013-10-06	04:07:25	3300	1.414	1.5	240	242
2013-10-07	04:01:37	3600	1.424	1.5	241	242
2013-10-07	05:05:37	3300	1.178	1.5	231	236

Table 3 — *Continued*

UT Date	UT Time	t_{int} (s)	sec(z)	slit width (")	slit angle (°)	par. angle (°)
2010-02-16	06:01:20	1800	1.730	0.7	196	203
2010-02-16	06:32:07	1800	1.639	0.7	196	195
2010-02-16	07:05:56	3600	1.590	0.7	177	186
2010-02-16	08:11:06	3000	1.626	0.7	160	167
2010-02-17	05:32:21	3600	1.845	0.7	202	209
2010-02-17	06:37:11	3600	1.621	0.7	185	192
2010-02-17	07:43:53	3600	1.594	0.7	166	174
2010-02-17	08:44:36	1800	1.731	0.7	166	158
SGAS J142954.9+120239						
2013-05-04	03:13:58	3600	1.399	1.0	195	202
2013-05-04	04:19:51	3600	1.326	1.0	173	182
2013-05-06	03:41:45	3600	1.342	1.0	183	191
2013-05-06	04:45:15	4500	1.338	1.0	162	171
2014-05-30	00:31:40	3600	1.617	2.0	212	217
2014-05-30	01:36:12	3600	1.391	2.0	193	201
2014-05-31	00:45:13	3600	1.535	2.0	207	213
2014-05-31	01:47:00	3600	1.365	2.0	188	197
2014-05-31	02:49:03	3600	1.327	2.0	167	177
SGAS J145836.1–002358						
2013-08-09	23:38:43	2700	1.20	2.0	143	151
2013-08-10	00:29:01	2700	1.32	2.0	132	137
2013-08-10	23:32:16	2700	1.19	2.0	143	152
2013-08-11	00:20:52	2700	1.31	2.0	133	138
2014-05-30	02:40:12	3600	1.149	2.0	182	194
2014-05-30	03:44:19	3600	1.151	2.0	155	166
2014-05-30	04:46:18	3600	1.245	2.0	137	144
2014-05-31	03:53:38	3600	1.163	2.0	150	160
2014-05-31	04:55:43	3600	1.280	2.0	134	140
SGAS J152745.1+065219 bright						
2008-02-08	08:49:42	900	1.479	2.0	213	219
2008-07-30	01:23:08	1800	1.386	2.0	282	326
2008-07-30	01:55:14	1800	1.515	2.0	282	319
2008-07-30	23:27:11	1800	1.235	2.0	177	183
2008-07-30	23:59:37	1800	1.242	2.0	177	171
2008-07-31	23:52:11	3600	1.240	2.0	163	172
2008-08-01	01:00:23	3600	1.343	2.0	144	150
2008-08-01	02:06:54	1812	1.624	2.0	132	136
2009-04-22	05:46:55	3600	1.240	2.0	180	188
2009-04-22	06:47:31	1800	1.253	2.0	180	166
2015-06-10	00:39:05	3900	1.525	1.0	216	222
2015-06-10	01:44:28	3900	1.305	1.0	216	206
SGAS J152745.1+065219 faint tail						
2015-06-13	01:10:54	3000	1.358	2.0	207	212
2015-06-13	02:05:59	3000	1.254	2.0	186	195
2015-06-13	03:13:17	2940	1.243	2.0	162	170
2015-06-14	00:45:52	3600	1.427	2.0	210	217
2015-06-14	01:46:58	3000	1.273	2.0	210	200
2015-06-14	02:38:03	2800	1.234	2.0	210	182
SGAS J211118.9–011431						
2013-08-10	01:36:17	3600	1.610	2.0	230	233
2013-08-10	02:40:16	3600	1.300	2.0	216	223
2013-08-10	03:46:00	4500	1.160	2.0	193	203
2013-10-05	23:56:07	3600	1.167	1.5	197	206
2013-10-06	00:59:14	3600	1.130	1.5	165	178
2014-05-30	06:05:56	3600	1.721	2.0	232	235
2014-05-30	07:08:42	3600	1.353	2.0	220	226
2014-05-30	08:11:30	3600	1.186	2.0	199	210
2014-05-30	09:13:58	1300	1.131	2.0	171	185
2014-05-31	06:27:38	3600	1.535	2.0	228	232
2014-05-31	07:29:40	3600	1.270	2.0	213	221
2014-05-31	08:31:26	2700	1.154	2.0	189	201
2014-05-31	09:18:02	2700	1.130	2.0	167	181
Cosmic Eye						
2008-07-28	03:04:54	1800	1.520	2.0	229	231
2008-07-28	03:36:57	1800	1.363	2.0	229	226
2008-07-28	06:19:28	1600	1.140	2.0	158	168
2008-07-28	06:48:40	1800	1.166	2.0	158	156

Table 3 — *Continued*

UT Date	UT Time	t_{int} (s)	$\sec(z)$	slit width (")	slit angle ($^{\circ}$)	par. angle ($^{\circ}$)
2008-07-28	07:25:19	1800	1.230	2.0	137	144
2008-07-28	07:56:00	1800	1.317	2.0	137	137
2008-07-31	03:24:03	1800	1.368	2.0	224	226
2008-07-31	03:55:23	1800	1.263	2.0	224	220
2008-07-30	03:08:19	1800	1.458	2.0	226	230
2008-07-30	03:39:52	1800	1.323	2.0	226	224
2008-07-30	04:15:15	1800	1.224	2.0	208	216
2008-07-30	04:45:41	1800	1.171	2.0	208	206
2008-07-30	05:30:14	1800	1.135	2.0	179	187
2009-04-22	08:49:11	1800	1.811	2.0	233	235
2009-04-22	09:20:07	1800	1.564	2.0	233	232
2009-04-23	08:59:02	1800	1.688	2.0	231	234
2009-04-23	09:34:03	1800	1.460	2.0	225	230
2009-04-24	09:23:29	2400	1.496	2.0	227	231
SGAS J224324.2–093508						
2012-08-19	02:10:39	3600	1.603	1.0	239	240
2012-08-19	03:15:51	3600	1.266	1.0	230	234
2012-08-19	04:18:14	3600	1.116	1.0	208	220
2012-08-19	05:25:13	3600	1.061	1.0	168	186

Note. — Columns are Universal date and time, integration time in seconds, $\sec(z)$ airmass, slit width in arcseconds, position angle of the slit (degrees east of north), and parallactic angle (degrees east of north). Times, airmasses, and parallactic angles are given for the start of each exposure.

Table 4
Redshifts for the MEGaSAURA sample.

Source name	z_{stars}	σ	z_{neb}	σ	z_{ISM}	σ	Notes
SGAS J000451.7–010321	1.6812	0.0003	1.681100	0.000100	1.680100	0.0020	z_{neb} from Rigby14
SGAS J003341.5+024217	2.3900	0.0010	2.388770	0.000150	2.388150	0.0003	z_{neb} from C III]; z_{ism} from Si II 1526 & Al II 1670
SGAS J010842.2+062444	1.9099	0.0004	1.910210	0.000030	1.907600	0.0001	z_{neb} from Rigby14
RCSGA 032727–132609							
Knot E	1.7037	0.0004	1.703400	0.000140	1.702300	0.0001	z_{neb} from Rigby14
Knot U	1.7038	0.0007	1.703884	0.000007	1.702400	0.0001	z_{neb} from NIRSPEC Rigby15
Knot G	1.7030	0.0010	1.703850	0.000050	1.702500	0.0001	z_{neb} from OSIRIS Rigby15
Knot B	—	—	1.703600	0.000070	1.702300	0.0002	z_{neb} from OSIRIS Rigby15
counterarc	—	—	1.703070	0.000060	1.702500	0.0004	z_{neb} from C III]; z_{ism} from Si II 1304 & Al II 1670
SGAS J090003.3+223408	2.0323	0.0005	2.032600	0.000100	2.031700	0.0001	z_{neb} from C III] replaces Rigby15
SGAS J095738.7+050929	1.8205	0.0007	1.820420	0.000040	1.820100	0.0002	z_{neb} from Rigby+14
SGAS J105039.6+001730	—	—	3.625300	0.000800	3.625400	0.0006	z_{ism} from Bayliss14; z_{neb} from Bayliss14
Cosmic Horseshoe SE	2.3814	0.0005	2.381150	0.000120	2.379250	0.0003	z_{neb} from Quider+09
SGAS J122651.3+215220	2.9252	0.0009	2.926000	0.000200	2.922900	0.0001	z_{neb} from noisy C III], replaces Rigby15
SGAS J142954.9+120239	2.8241	0.0006	2.824500	—	2.822300	0.0001	z_{neb} not well constrained
SGAS J145836.1–002358	3.4870	0.0010	3.486800	0.000200	3.484950	0.0002	z_{neb} from FIRE, H β , [O III] 5007 Å
SGAS J152745.1+065219							
bright	2.7627	0.0007	2.762280	0.000080	2.760650	0.0003	z_{neb} from C III], replaces Rigby15
faint tail	2.7627	0.0007	2.762800	0.000100	2.760100	0.0003	z_{neb} from C III]
SGAS J211118.9–011431	2.8590	0.0010	2.857700	—	2.858300	0.0007	z_{neb} not well constrained
Cosmic Eye	3.0734	0.0004	3.073500	0.000240	3.072358	0.0003	z_{neb} & z_{ism} from Quider10; multiple z_{ISM} components
SGAS J224324.2–093508	—	—	—	—	2.080000	0.0200	Broad-line AGN. Possible intervening C IV at $z = 2.057$

Note. — Columns are: 1) source name, 2)–3) stellar redshift and its uncertainty, 4)–5) nebular redshift and its uncertainty, 6)–7) redshift of the interstellar medium and its uncertainty, and 8) Notes on the source of the redshift measurement.